AGU PUBLICATIONS

Tectonics

RESEARCH ARTICLE
10.1002/2014TC003661

Key Points:
- Physical properties of the crust across the Central Iberian Zone
- Increase in crustal thickness
- Lateral change in crustal composition

Correspondence to:
R. Carbonell,
ramon.carbonell@csic.es

Citation:
Ehsan, S. A., R. Carbonell, P. Ayarza, D. Martí, D. Martínez Poyatos, J. F. Simancas, A. Azor, C. Ayala, M. Torné, and A. Pérez-Estaún (2015), Lithospheric velocity model across the Southern Central Iberian Zone (Variscan Iberian Massif): The ALCUDIA wide-angle seismic reflection transect, *Tectonics*, *34*, 535–554, doi:10.1002/2014TC003661.

Received 20 JUN 2014
Accepted 11 FEB 2015
Accepted article online 14 FEB 2015
Published online 23 MAR 2015

Lithospheric velocity model across the Southern Central Iberian Zone (Variscan Iberian Massif): The ALCUDIA wide-angle seismic reflection transect

Siddique Akhtar Ehsan[1], Ramon Carbonell[1], Puy Ayarza[2], David Martí[1], David Martínez Poyatos[3], José Fernando Simancas[3], Antonio Azor[3], Concepción Ayala[1,4,5], Montserrat Torné[1], and Andrés Pérez-Estaún[1]

[1]Department of Structure and Dynamics of the Earth, Institute of Earth Sciences Jaume Almera-CSIC, Barcelona, Spain, [2]Department of Geology, University of Salamanca, Salamanca, Spain, [3]Department of Geodynamics, Faculty of Sciences, University of Granada, Granada, Spain, [4]Instituto Geológico y Minero de España, Madrid, Spain, [5]Now at the Department of Structure and Dynamics of the Earth, Institute of Earth Sciences Jaume Almera-CSIC, Barcelona, Spain

Abstract A *P* wave seismic velocity model has been obtained for the Central Iberian Zone, the largest continental fragment of the Iberian Variscan Belt. The spatially dense, high-resolution, wide-angle seismic reflection experiment, ALCUDIA-WA, was acquired in 2012 across central Iberia, aiming to constrain the lithospheric structure and resolve the physical properties of the crust and upper mantle. The seismic transect, ~310 km long, crossed the Central Iberian Zone from its suture with the Ossa-Morena Zone to the southern limit of the Central System mountain range. The energy generated by five shots was recorded by ~900 seismic stations. High-amplitude phases were identified in every shot gather for the upper crust (Pg and PiP) and Moho (PmP and Pn). In the upper crust, the *P* wave velocities increase beneath the Cenozoic Tajo Basin. The base of the upper crust varies from ~13 km to ~20 km between the southernmost Central Iberian Zone and the Tajo Basin. Lower crustal velocities are more homogeneous. From SW-NE, the traveltime of PmP arrivals varies from ~10.5 s to ~11.8 s, indicating lateral variations in the *P* wave velocity and the crustal thickness, reflecting an increase toward the north related with alpine tectonics and the isostatic response of the crust to the orogenic load. The results suggest that the high velocities of the upper crust near the Central System might correspond to igneous rocks and/or high-grade metamorphic rocks. The contrasting lithologies and the increase in the Moho depth to the north evidence differences in the Variscan evolution.

1. Introduction

One of the most important and socially relevant objectives in Solid Earth Sciences is the knowledge of the relief/topography changes and their causes. Quite often, changes in topography are the direct result of the crustal response to the interaction between deep and surface processes (including erosion and, therefore, climate). However, the crustal response to these processes is controlled by its shallow and deep structure and by its physical properties. The rocks in the shallow crust are accessible by drilling, whereas at deeper crustal levels rocks can only be investigated by indirect techniques. It is, thus, mandatory to carry out an indirect probing of the deepest parts of the crust to understand its shallowest expression, the topography.

The evolution of the topography has been a major concern in Europe during the last decade, with numerous international research programs aimed to address this topic of high significance to society (e.g., TOPOEUROPE, [*Cloetingh et al.,* 2007]; TOPOMOD, [*Artemieva*, 2007]; and TOPOIBERIA [*Carbonell and TOPOIBERIA WG*, 2006]). In the Iberian Peninsula, the central meseta features an average altitude of 600–700 m and is actively increasing its elevation [*Cloetingh et al.,* 2011]. The way these changes are accommodated is highly dependent and very much related to the internal structure and physical properties of the crust, including crustal thickness. Since the early 2000s, the Spanish Earth Science research community has struggled to undertake multidisciplinary studies of the crust and lithosphere in SW and central Iberia. Detailed lithospheric structures have been delineated primarily from controlled source, high-resolution, normal incidence, and wide-angle seismic reflection data [*Simancas et al.,* 2003; *Carbonell et al.,* 2004; *Flecha et al.,* 2009; *Palomeras et al.,* 2009, 2011a; *Martínez Poyatos et al*., 2012; *Ehsan et al.,* 2014]. This manuscript aims to contribute to this knowledge providing additional information about central Iberia, aiming to add constraints that can be used in the study of the origin and evolution of its relief.

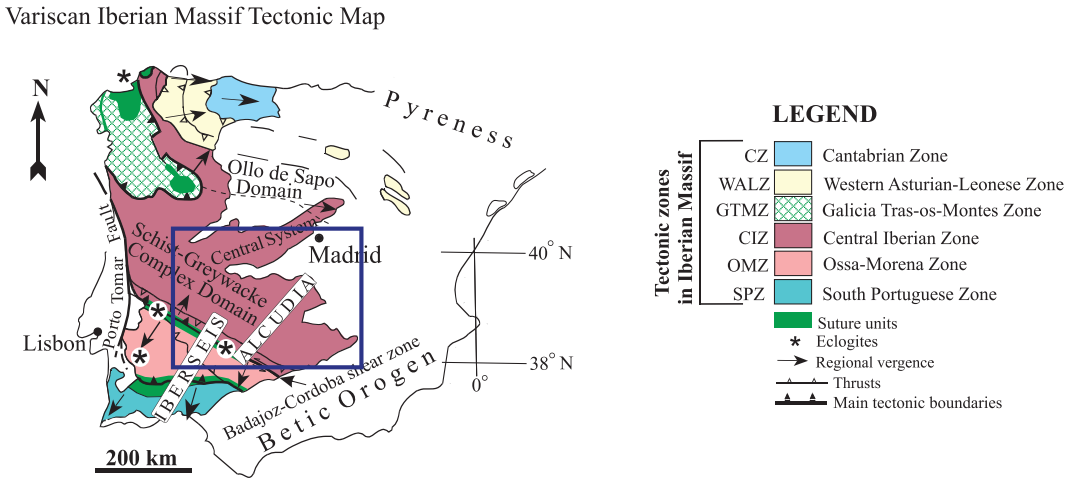

Figure 1. Map indicating the location of the study area (blue rectangle) within the Iberia. The location of normal incidence and wide-angle profiles (IBERSEIS and ALCUDIA) is indicated over the tectonic map of the Iberian massif. The study area, highlighted by a blue rectangle, is presented in more detail in Figures 2a and 3.

The geological processes at lithospheric scale are best understood by the high-resolution results obtained from deep seismic surveys. The main source of information about the physical properties and composition of the crust and upper mantle comes from wide-angle reflection prospecting, whereas the normal incidence experiments constrain the internal fabric and geometry of the crustal structure. Multiseismic experiments include normal incidence and spatially dense wide-angle seismic reflection data. Since the late 1980s, these experiments are the main tool to obtain constraints and improve the knowledge on the structure and physical properties of the lithosphere [e.g., *Klemperer and Matthews*, 1987; *Freeman et al.,* 1988; *Pérez-Estaún et al.,* 1991, 1994, 1995; *Carbonell et al.,* 1996, 1998, 2000; *Ayarza et al.,* 1998, 2004; *Cook et al.,* 1999, 2010; *Onken et al.,* 2000]. In order to estimate the composition of the crust and even the lithosphere, the physical properties of rocks (*P* and *S* wave velocities and densities) measured in laboratories are compared with the ones derived from wide-angle seismic reflection data [e.g., *Hawman et al.,* 1990; *Palomeras et al.,* 2009, 2011a].

The objective of this manuscript is to present ALCUDIA wide-angle seismic reflection profile (ALCUDIA-WA), which was acquired across the central part of the Iberian Massif (Figures 1–3). This ~310 km long transect starts at the boundary with the Ossa-Morena Zone (OMZ) and goes across the Central Iberian Zone (CIZ) until the Central System (CS) mountain range. The Iberia deep seismic reflection profile (IBERSEIS) normal incidence and wide-angle seismic reflection data [*Simancas et al.,* 2003; *Carbonell et al.,* 2004; *Flecha et al.,* 2009; *Palomeras et al.,* 2009, 2011a] were acquired in the southwestern part of the Iberian Peninsula (Figure 1). The ALCUDIA normal incidence and wide-angle seismic reflection data constitute the northern extension of the IBERSEIS seismic experiments (Figure 1). The ALCUDIA normal incidence deep seismic reflection transect (ALCUDIA-NI) provided high-resolution structural image of the crust and upper mantle [*Martínez Poyatos et al*., 2012; *Ehsan et al.,* 2014]; however, the physical properties (*P* and *S* wave velocities and densities) and composition of the crust were not constrained by this seismic experiment. This implies that previous estimations of the crustal thickness lack the constraints that allow time to depth conversion of seismic data sets and gravity modeling of Bouguer anomaly data. However, the calculation of the crustal thickness is the key to understand the increase in the topography as we approach the CS mountain range. The present analysis of the ALCUDIA-WA data places unique constraints on the physical properties and composition of the crust of the CIZ (Figures 2b and 3). The main objectives of ALCUDIA-WA are (1) to derive a well-resolved *P* wave velocity model, (2) to place key constraints on the nature and composition of the crust and upper mantle, (3) to provide insights on the large-scale structures/boundaries, (4) to determine the crustal thickness based on the reflections associated with the crust-mantle boundary, and (5) to assess the implications of the previous points into the tectonics and evolutionary processes of the lithosphere and its topography. In summary, the ALCUDIA-WA provides an excellent opportunity to study the distribution of physical properties of an old intracontinental orogenic region with limited knowledge on the nature of the structures below the surface.

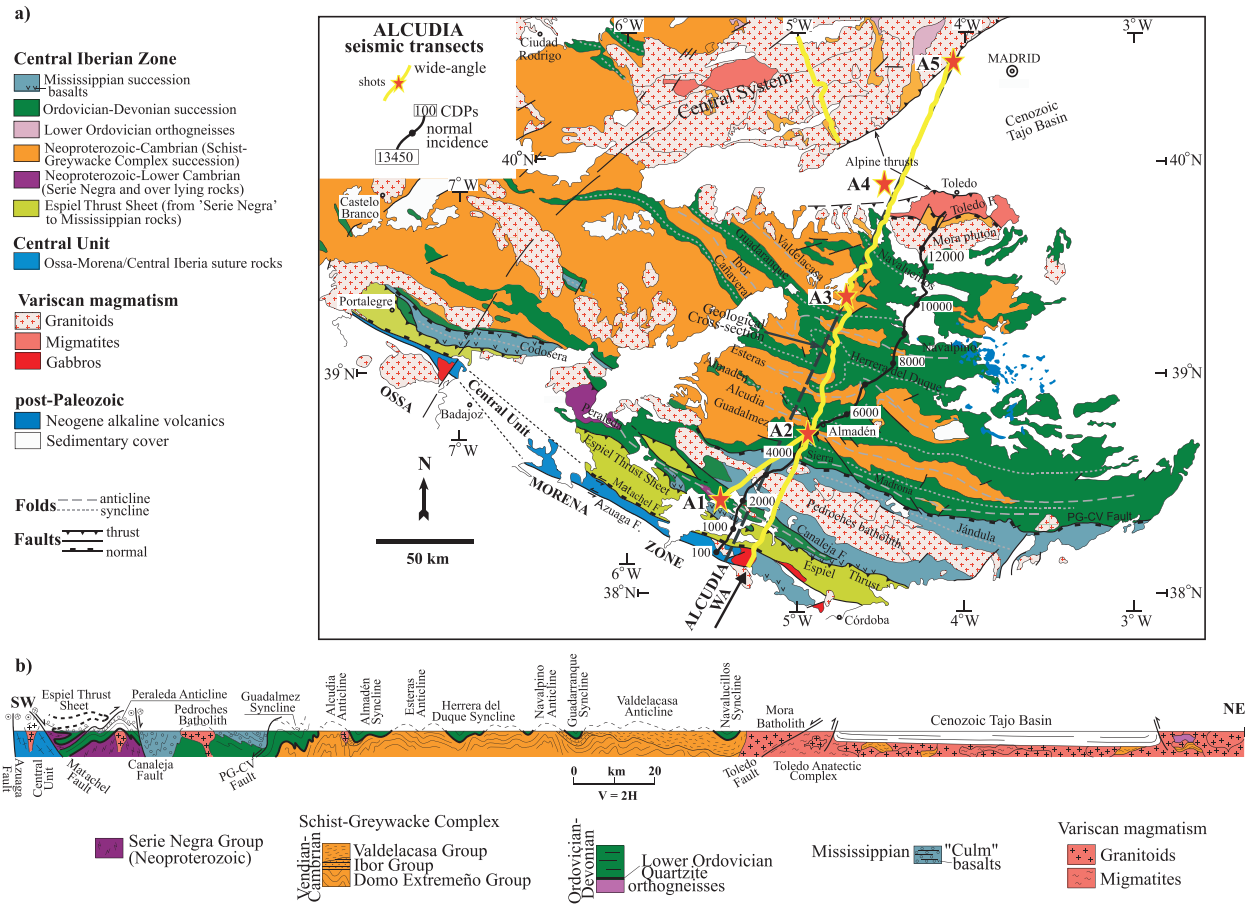

Figure 2. (a) Geological map of the survey area with the layout of the ALCUDIA-NI and ALCUDIA-WA seismic reflection profiles. The shot locations (A1 to A5) and Common Depth Point (CDPs) are also indicated along both seismic data sets. The main ALCUDIA-WA transect selected for *P* wave velocity model is also marked. (b) Geological cross section along the dashed gray line in the map. The surface geological cross section is derived from the data collected in the field.

2. Geological and Geophysical Setting

The Iberian Massif represents an almost continuous section of the so-called Variscan-Alleghanian orogen, which resulted from Late Paleozoic collision between two main paleocontinents: Laurentia-Baltica to the north and Gondwana to the south [*Franke*, 2000; *Matte,* 1986, 2001]. The Iberian Massif is made up of six continental fragments, some of them with suture units in between (Figure 1). The Cantabrian Zone and the South Portuguese Zone (SPZ) represent the external zones, while the Western Asturian-Leonese Zone, the Galicia-Tras-os-Mostes Zone, the CIZ, and the OMZ are the internal zones of the Iberian Massif (Figure 1) [e.g., *Simancas et al.,* 2001, 2003]. The CIZ is bounded to the south by the Badajoz-Cordoba Shear Zone [*Burg et al.,* 1981], later redefined as the Central Unit (CU) [*Azor et al.,* 1994]. It is a 5 km wide zone considered to be the tectonometamorphic boundary between the CIZ and the OMZ, i.e., its suture. It is limited to the south by the Azuaga fault and to the north by the Matachel fault (Figures 2a and 2b).

The main geological features of the CIZ include [*Martínez Catalán et al.,* 2004] (1) Neoproterozoic to Lower Cambrian flysch sedimentary successions (Schist-Greywacke Complex, Serie Negra) related to the Cadomian orogeny along northern Gondwana, (2) Lower Ordovician orthogneisses (continental rifting), (3) Ordovician to Devonian succession (continental platform), (4) Devonian to Carboniferous deformation and metamorphism (Variscan collision), (5) Mississippian flysch succession related to intracollisional extension, and (6) Pennsylvanian migmatites and granitic batholiths (syn to late Variscan orogeny). The CIZ is subdivided into two tectonic domains [*Martínez Catalán et al.,* 2004]: (1) in the north, the Ollo de Sapo Domain is characterized by Lower Ordovician glanular gneisses and Variscan recumbent folds; (2) in the south, the Schist-Greywacke Complex Domain is characterized by a thick Neoproterozoic-Lower Cambrian flysch sedimentary succession and Variscan upright folds. The ALCUDIA-WA samples a complete transect of the Schist-Greywacke Complex Domain

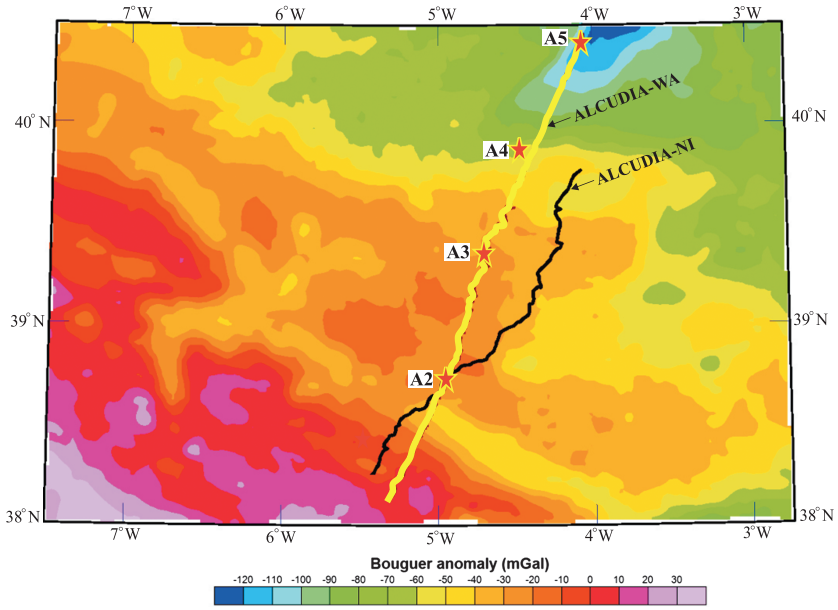

Figure 3. Bouguer gravity anomaly map of the survey area showing the location of the ALCUDIA-NI and ALCUDIA-WA seismic reflection profiles. The shots point locations of the latter are also indicated.

(Figures 1, 2a, and 2b). Toward the north, it is covered by the Tajo Basin (TB), a Cenozoic fore deep of the CS, an Alpine mountain range [*de Vicente and Muñoz-Martín*, 2013].

SW Iberia has been sampled by controlled-source seismic reflection experiments that include normal incidence [*Simancas et al.,* 2003; *Carbonell et al.,* 2004; *Martínez Poyatos et al*., 2012; *Ehsan et al.,* 2014] and wide angle [*Palomeras et al.,* 2009, 2011a]. These were acquired within two main research programs: The IBERSEIS and the ALCUDIA projects [*Simancas et al.,* 2003; *Carbonell et al.,* 2004; *Martínez Poyatos et al*., 2012; *Ehsan et al.,* 2014]. Together, they constitute an almost 600 km long crustal transect aimed to address the crustal structure and the physical properties of the central and the SW Iberian Massif. The images obtained from IBERSEIS and ALCUDIA normal incidence profiles reveal that the crust is more reflective than the upper mantle [*Simancas et al.,* 2003; *Carbonell et al.,* 2004; *Martínez Poyatos et al*., 2012; *Ehsan et al.,* 2014]. The crustal internal architecture is variable, thus suggesting the existence of a number of different processes, lithologies, and terranes across the SW Variscan orogen. However, common features exist in both transects: (1) a prominent boundary between the upper crust and the mid-lower crust and (2) a clear Moho discontinuity located at 10 s to 11 s two-way traveltime (twtt) [*Simancas et al.,* 2003, Figure 3; *Martínez Poyatos et al*., 2012, Figure 4; *Ehsan et al.,* 2014, Figure 4]. Both discontinuities are suggested to act as decoupling surfaces [*Simancas et al.,* 2003; *Carbonell et al.,* 2004; *Martínez Poyatos et al*., 2012; *Ehsan et al.,* 2014]. The IBERSEIS normal incidence deep seismic reflection profile imaged a ~3–5 km (1–2 s) thick and ~175 km long, high-amplitude reflective band at midcrustal levels (~4.5 s twtt) [*Simancas et al.,* 2003, Figure 3]. This midcrustal, sill-like structure (IRB, the Iberseis Reflective Body) was interpreted as a layered magmatic body [*Simancas et al.,* 2003] intruded along the brittle/ductile transition and was not observed to the north, in the ALCUDIA-NI seismic section. In the latter, the most outstanding features are (1) a thick and very reflective mid-lower crust with ductile boudinage structures approximately 7 km long and (2) an upper mantle wedge [*Martínez Poyatos et al*., 2012; *Ehsan et al.,* 2014]. The seismic character in the vicinity of the crust-mantle transition is laterally variable: it changes from sharp, high-amplitude reflectivity beneath the SPZ to diffuse and discontinuous below the OMZ and to highly reflective again under the CIZ [*Simancas et al.,* 2003; *Carbonell et al.,* 2004; *Martínez Poyatos et al*., 2012; *Ehsan et al.,* 2014].

The IBERSEIS wide-angle seismic reflection experiment has proved to be very successful in placing constraints on the distribution of structures and physical properties in the upper lithosphere [*Flecha et al.,* 2009; *Ayarza et al.,* 2010; *Palomeras et al.,* 2011a]. It consisted of two profiles (A and B), ~250 and ~300 km long, respectively, one of them coincident with the IBERSEIS normal incidence experiment [*Palomeras et al.,* 2009, 2011a, Figure 1].

Table 1. Data Acquisition Parameters for ALCUDIA-WA Transect

Survey Parameters	
Type of survey	2-D crooked line
Recording system	IRIS-TEXANS (RT125A)
Nominal spread	Asymmetrical split spread
Energy Source Parameters	
Source type	Chemical explosive
Nominal shot depth	50–60 m
Nominal shot interval	60–80 km
Nominal shot size	1000 kg
Shot design	Single borehole
Total no. of shots	5 (1 TM each)
Recording Parameters	
Geophones	Single component, 10 Hz
Nominal active channels	900
Nominal receiver interval	340–600 m
Recording length	80 s
Sampling rate	4 ms
Total length	350 km

The Moho is located at ~32 km depth although some crustal thickening is depicted around the CU, coinciding with the location of the IRB. The structural image obtained from the IBERSEIS wide-angle, low-fold stack section, and from the synthetic modeling reveals a strongly heterogeneous crust and relatively complex structures for the crust-mantle transition beneath the OMZ when compared to the SPZ and the CIZ [*Flecha et al.,* 2009]. The *S* wave structure and Poisson's ratio models were calculated to place further constraints on the possible rock types that make up the crust in the SW Iberia [*Palomeras et al.,* 2011a, Figures 5 and 6]. Furthermore, multidisciplinary potential field lithospheric modeling that included gravity, heat flow, geoid, and topography provided further support to the crustal model and constrained the geometry of the lithosphere-asthenosphere boundary [*Palomeras et al.,* 2011b, Figures 4 and 5].

Different geophysical approaches have also been used to constrain the models derived from the IBERSEIS and ALCUDIA seismic experiments. A 200 km long magnetotelluric (MT) transect, overlapping the IBERSEIS normal incidence profile, was acquired across the SW Iberian Massif. The resulting models reveal distinctive electric conductivities for the SPZ, the OMZ, and the southern CIZ [*Pous et al.,* 2004, Figure 5]. A 120 km long high-conductivity layer extending along the OMZ coincides with the IRB at midcrustal depths, suggesting that the two are probably related [*Pous et al.,* 2004, Figure 3]. Another MT transect was acquired overlapping the ALCUDIA-NI profile [*Pous et al.,* 2011]. It featured distinctive upper crust conductive bodies that correlate with the surface geology, and a mild but persistent mid-lower crust conductivity layer. Bouguer gravity anomaly modeling [*Ayala*, 2013; *García-Lobón et al.,* 2014] has also provided additional control to the shallow crustal structure studied by the ALCUDIA-NI section.

The ~310 km long ALCUDIA-WA transect is the latest effort carried out to unravel the structure and composition of central Iberia. Acquired in spring 2012, it overlaps the trace of the ALCUDIA-NI transect (Figure 2a) providing the keys to establish the link between normal incidence time sections and depth sections. The integration of both data sets will contribute to establish a structural and compositional model of this internal area of the Iberian Massif, in the same way that the IBERSEIS transects achieved it for the SPZ and the OMZ.

3. The ALCUDIA Wide-Angle Seismic Reflection Profile: *P* Wave Data

3.1. Acquisition

The acquisition design included three lines of receivers, having a total length of ~350 km (Figure 2a). The main line, the so-called ALCUDIA-WA (Figures 2 and 3), is ~310 km long strikes NE-SW to NNE-SSW, it is approximately perpendicular to the structural grain. A ~40 km long line of receivers that trends NNW-SSE was deployed perpendicular to the CS mountain range. Over 900 TEXANS (single component, digital recording seismic station) from the IRIS-PASSCAL Instrument Pool were deployed from the northern boundary of the OMZ to the alpine thrust representing the southern boundary of the CS (Figure 2a). The entire ALCUDIA-WA survey had a nominal shot and receiver spacing of 70 km and 400 m, respectively. Five explosive sources (A1 to A5, Figure 2a), each one consisting in 1 TM of explosive, were placed in ~55 m deep single boreholes (Table 1), providing a signal rich in high frequencies resulting in shot records characterized by high signal-to-noise ratio. For this reason, these data can be qualified as a high-resolution wide-angle data set. This manuscript analyzes the data provided by four shots of the ALCUDIA-WA main transect (Figures 2a and 3). The acquisition geometry with regard to shot A1 (Figure 2a) can introduce

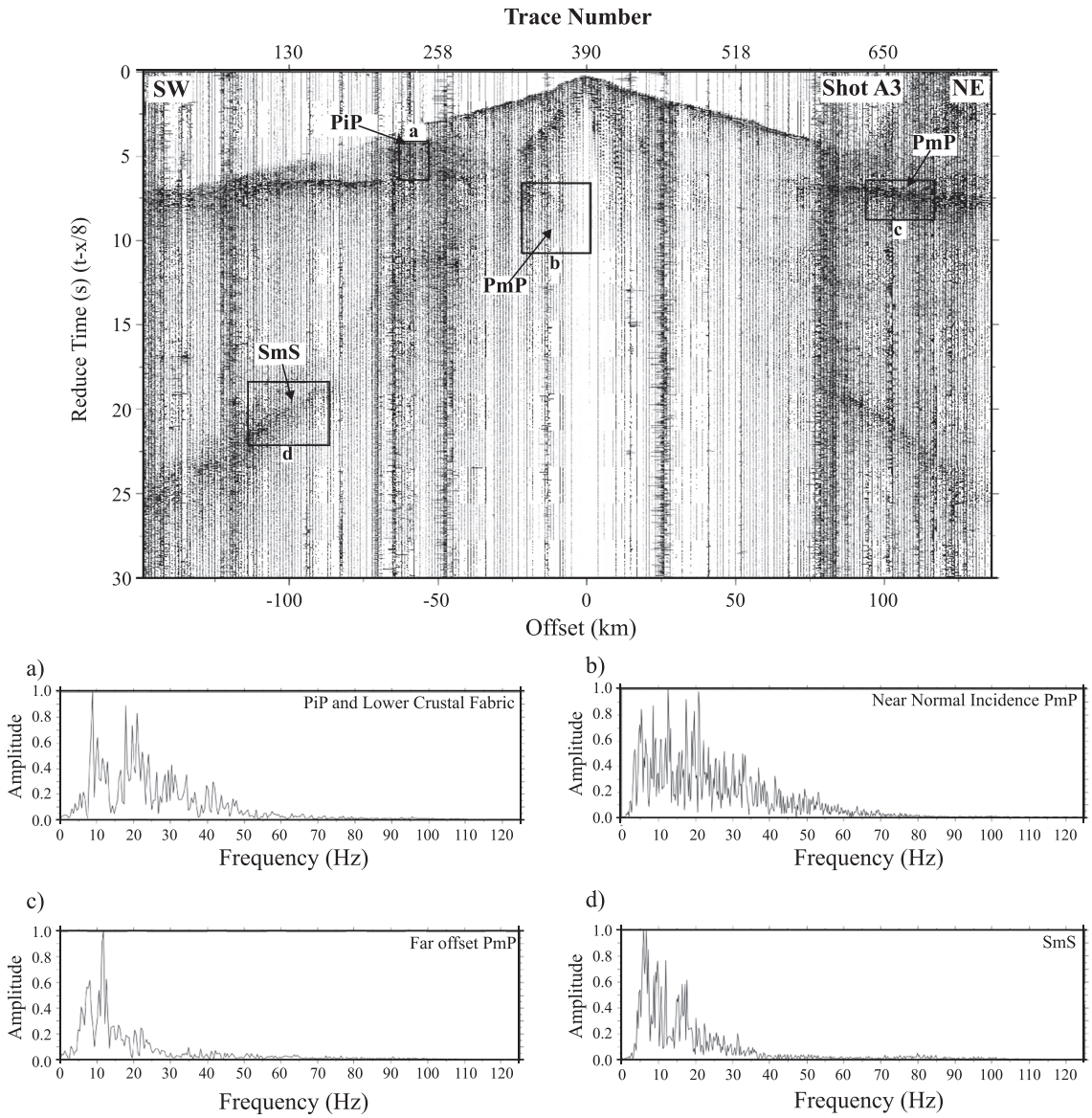

Figure 4. (a–d) Example of amplitude spectra of the main seismic events (interpreted as PiP, PmP, and SmS) for raw shot gather A3. The shot gather is displayed with a reduction velocity of 8.0 km/s. Note the wide range of frequencies present in PiP (Figure 4a) and its reverberative character. In general, high amplitudes exist up to frequencies of 20 Hz.

traveltime complexities and uncertainties in the quantitative interpretation. Therefore, shot gather A1 was excluded in the current contribution and only shot gathers A2–A5 are considered in the numerical modeling.

3.2. Processing

For the purpose of phase identification and traveltime picking, raw and processed shot records were analyzed throughout processing. The main focus of the processing was to enhance the *P* wave phases, and, for the purpose of this manuscript, special attention was paid to the first 30 s of the shot records. The processing included amplitude corrections for spherical spreading (amplitude gain and scaling), analysis of the frequency content in order to design appropriate band-pass filters (Figure 4), and amplitude balancing. A reduction velocity of 8.0 km/s was used for display purposes (Figures 4–7).

Frequency analysis reveals that different crustal *P* wave events present on the shot records feature frequencies from 4 to 25 Hz (Figures 4 and 5). The main phases, PmP and PiP, have frequencies between 10 and 20 Hz but are already resolved by low-frequency band-pass windows, from 2 to 8 Hz and from 2 to 13 Hz,

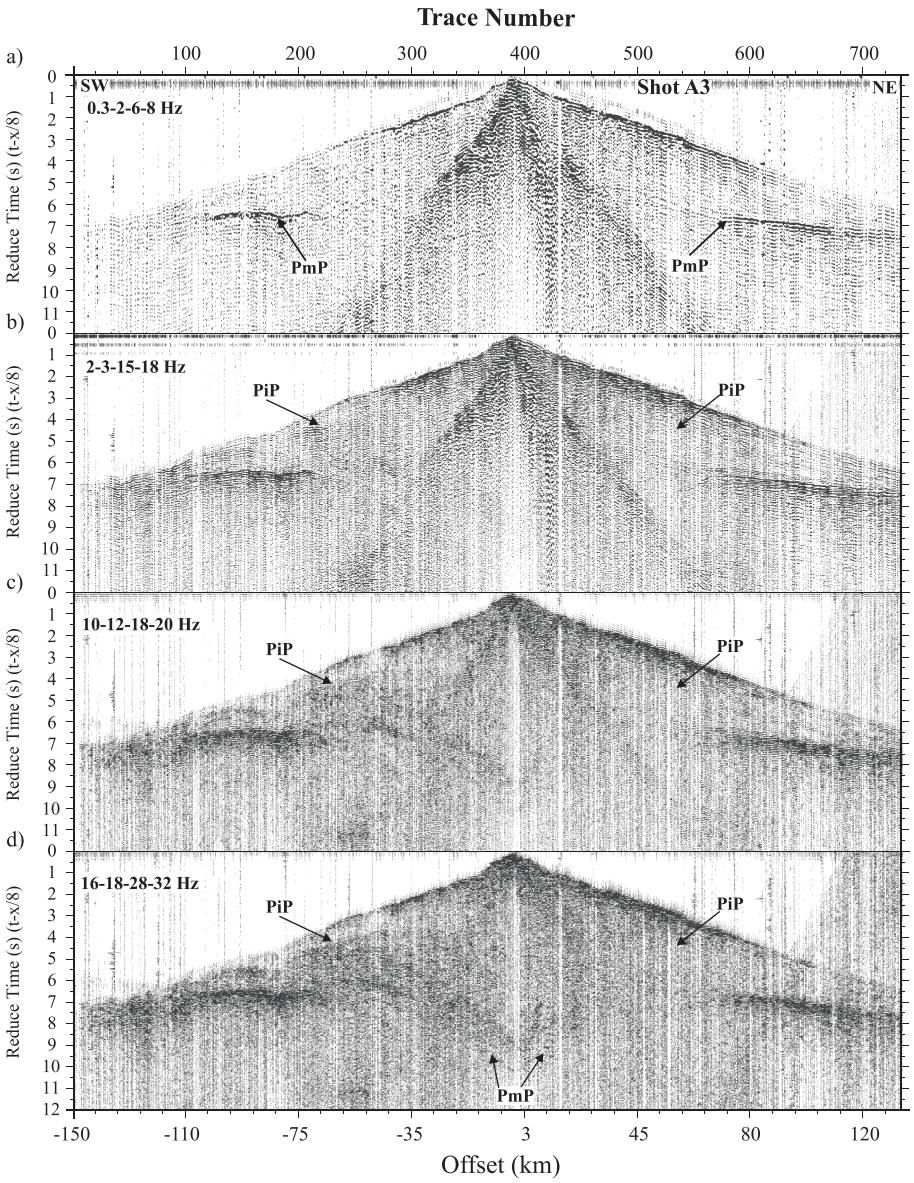

Figure 5. Band-pass filter panels applied over shot A3 with a reduction velocity of 8.0 km/s. (a) Frequency filter: 0.25, 2, 6, 8 Hz shows already a very conspicuous PmP, (b) frequency filter: 6, 8, 12, 15 Hz brings out PiP, (c) frequency filter: 10, 12, 18, 20 Hz, and (d) frequency filter: 18, 20, 30, 35 Hz shows the very reflective character of the crust between PiP and PmP. At the low frequency in Figures 5a and 5b, phases can be interpreted only at far offsets. In the highest frequency in Figures 5c and 5, an almost continuous band of reflectivity is observed between PiP and PmP from normal incidence to far offsets.

respectively (Figures 5a and 5b). As the width of the band-pass filter is increased, the imaged events reveal much of the associated coda, suggesting a notable increase in the structural complexity. Note, for example, that the reflectivity just beneath the PiP is enhanced when a band-pass filter of 10–20 Hz or 16–32 Hz is applied, suggesting a laminated structure between PiP and PmP. Furthermore, when high frequencies are considered, the PmP arrival can be identified at normal incidence (Figures 5c and 5d). This unusual observation in wide-angle shot records is possible, thanks to the narrow trace spacing and the bandwidth of the seismic source, and will contribute greatly to define the Moho. For the conventional model interpretation, a band-pass filter between 5 and 20 Hz (5–8–18–20 Hz) was applied to the shot records in order to reduce source-generated noise, to improve the data quality, and to enhance the reflectivity of the principal arrivals. The application of a predictive Wiener deconvolution using a 250 ms operator and a 16 ms gap length had a great influence on the resolution and helped to reduce the noise, whitening the frequency content of the seismic signal. After this

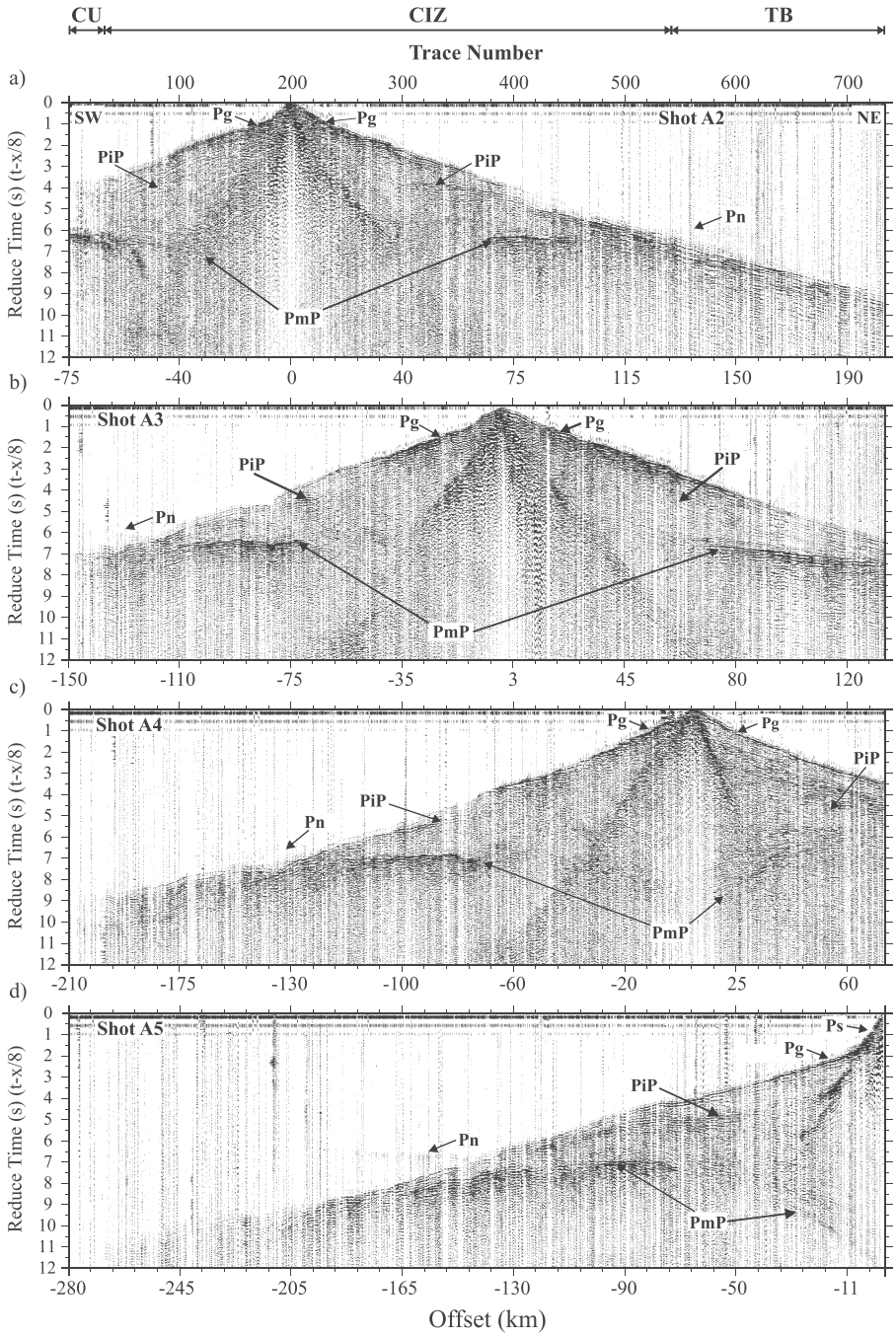

Figure 6. (a–d) The four shot gathers, from south to north, A2, A3, A4, and A5 across the main ALCUDIA-WA reflection transect. A band-pass filter from 5 to 20 Hz was applied to enhance the reflectivity of the main *P* wave arrivals (Pg, PiP, PmP, and Pn). Pg is the first *P* wave arrival, PiP is the *P* wave reflected phase at boundary between the upper and mid-lower crust, and PmP is the *P* wave reflected from the crust-mantle transition (Moho discontinuity). Pn is the *P* head wave traveling within the upper mantle. Data are displayed with a reduction velocity of 8.0 km/s to enhance the mantle phases.

processing sequence (Table 2), a series of high-amplitude events (retaining true relative amplitude information) are identifiable within the crust and down to Moho depths.

3.3. Data Description

The shot gathers (A2 to A5, from south to north, Figures 2a and 3) show good quality and clear *P* wave arrivals from the boundary between the upper and mid-lower crusts, the Moho and the upper mantle

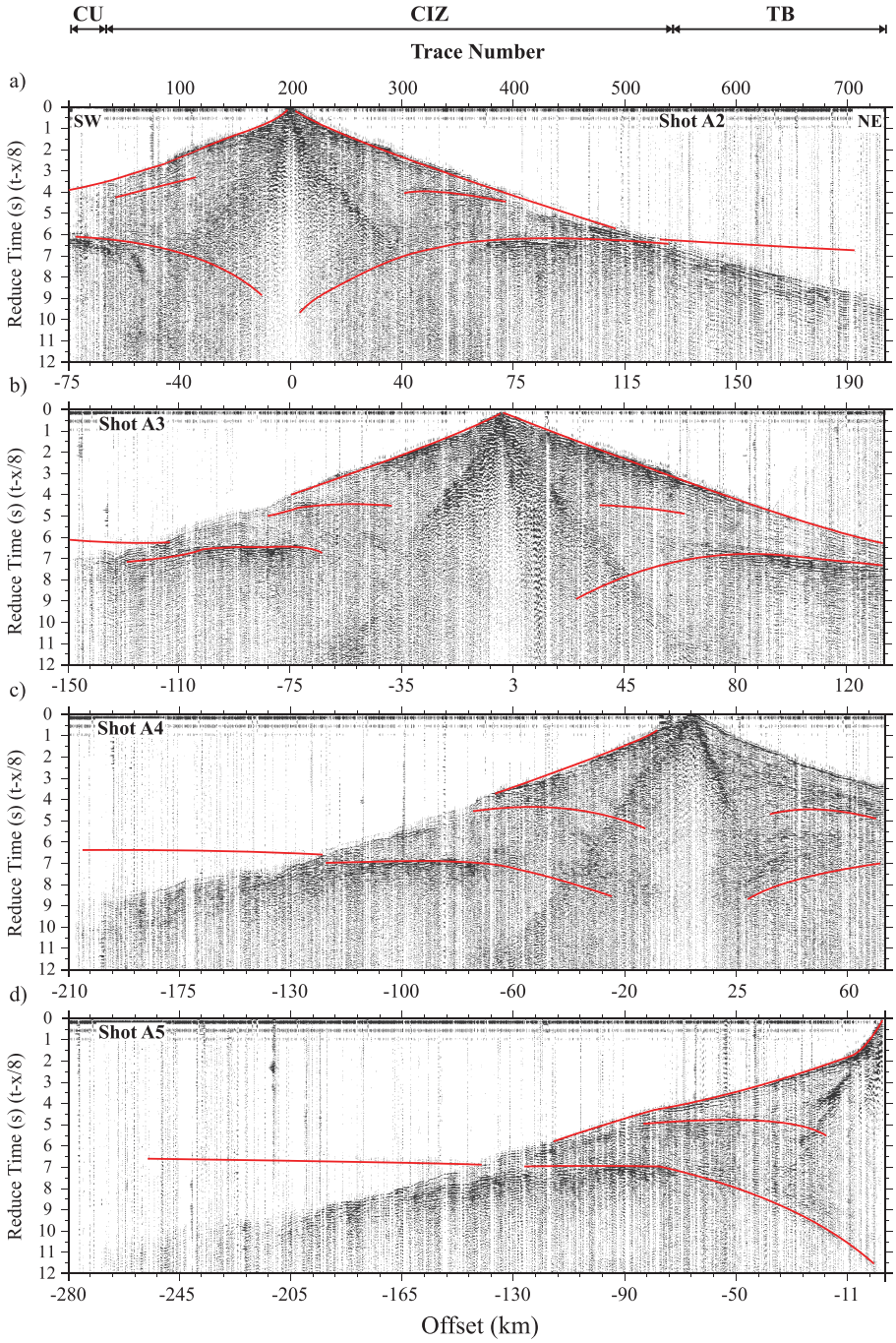

Figure 7. (a) Theoretical traveltime branches predicted by the *P* wave velocity model generated by the *Zelt and Smith* [1992] algorithm. A good fit exists between the observed phases and the model prediction. Reduction velocity is 8.0 km/s. The processing parameters for data are the same as in Figure 6. (b) Raypath coverage along the main ALCUDIA-WA. Ray coverage in the upper and mid-lower crust is good. The Moho discontinuity is sampled at normal incidence in shot A5. Upper mantle sampling gets down to 40–42 km. The ray tracing diagram shows the lack of rays for the southernmost edge of the profile.

(Figures 6a–6d). The presence of laterally limited events is occasional. The identified phases can be correlated from shot to shot and, therefore, are interpreted to correspond to the same structure or interface. The correlation is based on the similarities between time-offset relations and amplitudes of the events. The identified phases Ps, Pg, PiP, PmP, and Pn constrain a layered crustal model consisting of sediments, an upper crust, mid-lower crust, and mantle. Details in the slope of the direct arrivals, Ps and Pg,

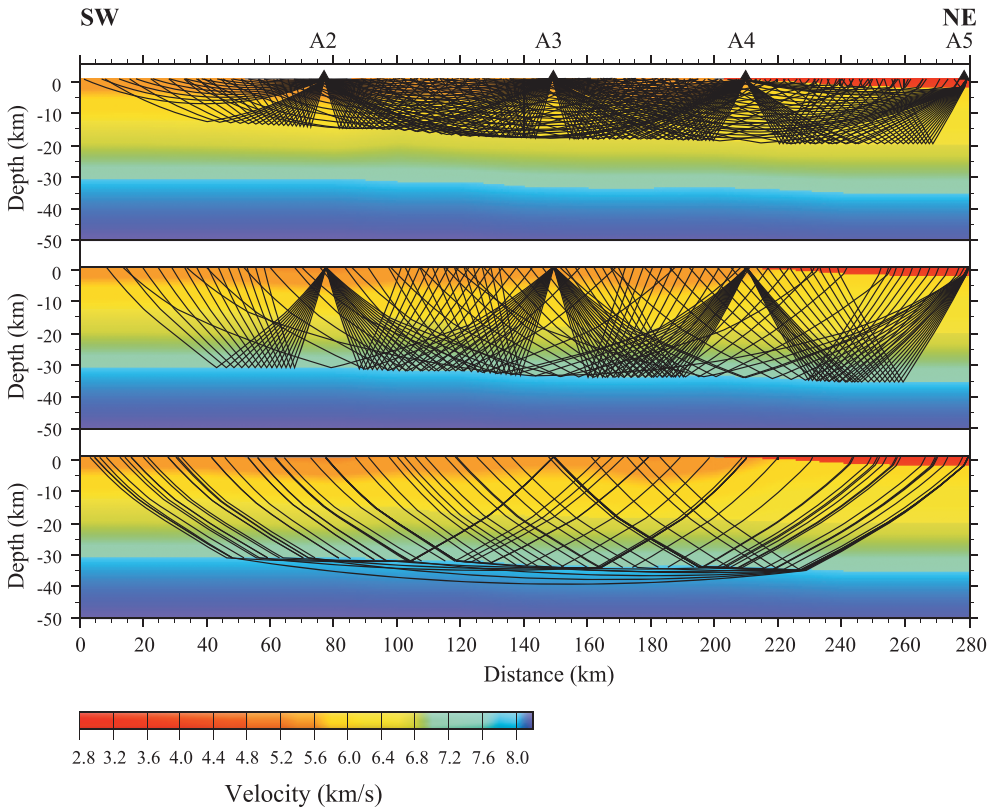

Figure 7. (continued)

are consistent with surface geology (Figures 2a and 2b). The direct arrivals and the reflected *P* wave arrivals at the Moho (PmP) are the most outstanding events (Figure 6). The Pg phase is observed up to large offsets, and the *P* wave reflected arrivals from the boundary between the upper and mid-lower crust (PiP) feature relatively high amplitudes. The PmP phase can be followed in all shot gathers from normal incidence to until ~120 km offset. A critical refraction at the Moho boundary through the upper mantle, the Pn phase, is identified for offsets larger than 120 km across all the shot gathers.

Note that for shot records A2 and A3, the observed PmP intercept time is ~10.5 s reduced traveltime (Figures 6a and 6b). However, shot gather A4 (Figure 6c) reveals a clear shift in arrival times for this phase at near offsets: for the southern branch, the PmP phase identified between −7 km to −13 km offsets shows reduced traveltimes of 9.5 s to 10.3 s. To the north, between +9 km to +15 km offsets, the observed reduced traveltimes are higher, varying from 10.9 s to 10.3 s. Finally, the recorded PmP phase intercept time for shot gather A5 is ~11.8 s. In summary, the intercept time of the PmP event varies from south to north between ~10.5 s and ~11.8 s. In the same way, the critical distances and times at which this phase is observed increase from 75 km and 6.2 s in shot A2 to almost 90 km and 7 s for shot A5. This implies that either the crust thickens or the velocities decrease from south to north. Also, the PmP phase features a ~1 s coda in all the shot records, suggesting the existence of reverberative structures at deep crustal levels. A clear subcrustal *P* wave refracted phase (Pn) is identified at far offsets (higher than 120 km). This phase

Table 2. The Principal Processing Parameters for ALCUDIA-WA Transect[a]

Processing Module	Parameters
1. Read SEGY formatted data SEGY	80 s
2. Band-pass filtering	5–8–18–20 Hz
3. Wiener deconvolution	Gap-deconvolution filter length 250 ms, gap length 16 ms 1% Prewhitening
4. SD compensation	Forward
5. Reduction velocity	8 km/s

[a]SEGY is a standard storage format developed by the Society of Exploration Geophysicist. SU Seismix Unix is a seismic reflection processing software package developed by the Colorado School of Mines. SD = Spherical divergence correction.

is more prominent in shot gathers A4 and A5, where it appears dipping to the near offsets, suggesting *P* wave apparent velocities above 8.0 km/s. These values could represent real *P* wave velocities above 8.0 km/s or a crustal thinning to the south.

3.4. Results: *P* Wave Seismic Velocity Model

A 2-D crustal velocity model was determined from the wide-angle shot records using *Zelt and Smith* [1992] ray tracing software. The algorithm follows a two-dimensional ray tracing approach that accounts for all arrivals in all shot records to compute a single *P* wave velocity model. To undertake the 2-D modeling, the source and receiver positions have been projected perpendicular onto a reference line containing offset information. The velocity and boundary nodes of the starting model were first defined, and an iterative method was adopted for the fast ray tracing traveltime computations. We pursued a simple layer stripping approach and began with Ps and Pg phases to place constraints on the shallowest segments of the velocity model. Then, the crustal phase (PiP), the Moho, and the upper mantle events were included in the model. The observed traveltimes were brought into agreement with calculated traveltimes by trial and error.

The resulting *P* wave velocity model is approximately 280 km long. Following the surface geology, it samples, from south to north (Figures 2a and 2b) the CU, the CIZ, and the TB. The *P* wave seismic velocity model (Figures 7b and 8b) has a layer cake velocity structure, which includes lateral velocity variations, mostly within the upper crust. This shallow velocity variations are consistent with surface geology and are well constrained down to ~20 km depth.

In the southern part of the velocity model (Figure 8b), the long Pg phase features changes in its slope that allow us to identify the presence of two layers in the upper crust; first a shallow ~5 km thick velocity gradient appears from 5.2 km/s to 5.8 km/s that could represent the CIZ low-grade metasediments. Then, from 5 km down to 13 km depths, the velocities increase up to 6.2 km/s and may correspond to the pre-Variscan basement. PiP constrains a relatively sharp velocity contrasts between this layer and the mid-lower crust, where the *P* wave seismic velocity jumps to values of 6.6 km/s. In addition, the coda shown by PiP in some shot gathers (e.g., A3 and A5, Figure 6) reveals a complex transition to the next layer. This interface increases in depth toward the north. At approximately 200 km from the southern end, it is located at 20 km depth. From this crustal level to the base of the crust, velocities increase from 6.6 km/s to 7.2 km/s. PmP constrains the position of the base of the crust between 31 and 32 km in this area with a sharp velocity increase from velocities of 7.1–7.2 km/s to values over 8.0 km/s. A conspicuous coda characterizes this phase in most shot gathers, also suggesting the existence of complex, reverberative structures in the lower crust and Moho.

To the north, the Ps and Pg phases identified in shot records A4 and A5 place constraints on the velocities that characterize the TB (Figure 8b). The relatively thick basin (2000 m on average, but up to 3800 m in areas close to the CS) [*de Vicente and Muñoz-Martín*, 2013] features average *P* wave seismic velocities close to 3–4 km/s. Velocities have a sharp increase to values of 6 km/s, typical of the basement, at depths over 2 km. From the base of the sedimentary basin to 15 km depth, the seismic data shows a relatively steep gradient where velocity exceeds values of 6.4 km/s in the limit with the lower crust. This part of the section also features a smooth increase in the depth of the Moho. Crustal thickness is calculated by inverted PmP phases at a depth of 35.5 km at the northern end of the transect. The lower crust occupies the interval between 20 and 35.5 km depth and shows velocities within the range of 6.6–7.2 km/s, similar to those found in the southern part of the section. Note that a significant lateral velocity variation has been constrained by the seismic data (Figures 7b and 8b) in the upper crust when taking into account the entire section. This is easily identifiable by following the trajectory of the 5.8–6.4 km/s isolines, from south to north. This gradient agrees with surface geology, which reveals that important lithological changes take place. Low-grade metasediments prevail in the uppermost crust for most of the profile. However, from the Mora pluton to the north, excluding the shallow TB, felsic to intermediate plutonic rocks and high-grade metamorphic rocks are the dominant lithologies. The change in *P* wave velocities is accompanied by a gradual increase in crustal thickness. Both features will be addressed in section 5.

3.5. Model Resolution and Uncertainties

The derived *P* wave velocity model (Figure 8b) reproduces the picked traveltime branches with a very good agreement (0.1–0.2 s, Figure 7a). The observed misfits are expectable since there are always factors that contribute to the mismatch between modeled and observed traveltimes, the most important of them being the acquisition geometry itself. The acquired data follows a crooked pattern that is later projected onto a

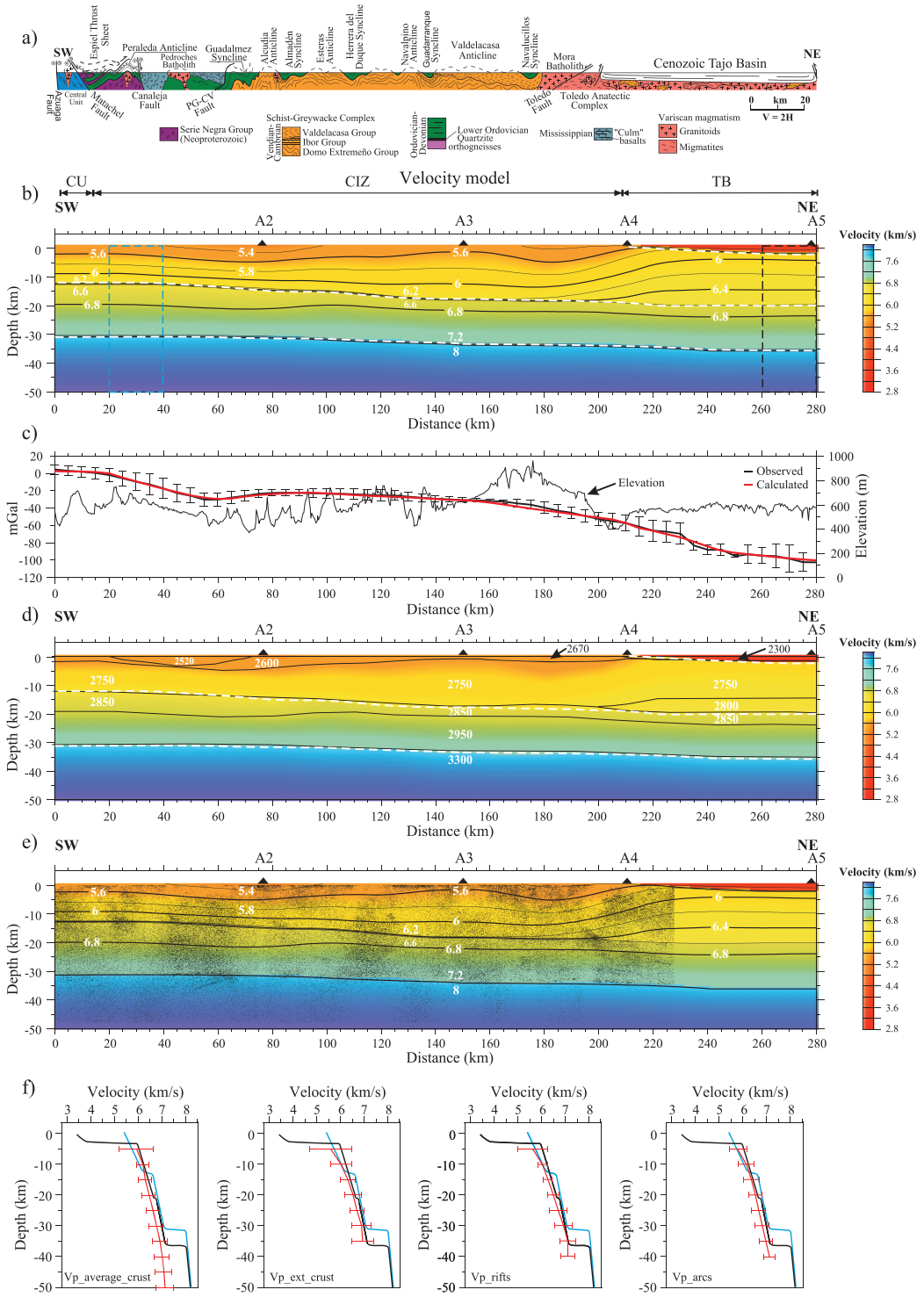

Figure 8. (a) Geological cross section and (b) crustal *P* wave velocity model for the main ALCUDIA-WA obtained by iterative (layer stripping) ray tracing. Two velocity-depth functions are estimated over the highlighted blue and black rectangles and are shown in Figure 8f. The major crustal interfaces are also highlighted (white dashed lines) on the models. (c) Observed (red line) and calculated (black line) Bouguer gravity anomaly along elevation profile and (d) derived crustal and upper mantle density model. Note that the conversion of *P* wave velocities to densities was done by using the empirical formulation from *Brocher* [2005]. It provides an almost perfect fit between the observed and the calculated Bouguer gravity anomaly. This complements the velocity model for a better lithological interpretation. (e) For the purpose of comparison, the ALCUDIA-NI profile, converted to depth using the *P* wave velocities obtained in this work, overlies the velocity model. Note the correlation (good fit) between the locations of the crustal interfaces (including the Moho) in both data sets. (f) The distribution of velocities (blue and black lines) derived from the 2-D velocity model from the main ALCUDIA-WA compared with standard velocity-depth functions (red line) for average continental crust, extended crust, rifts, and continental arcs [from *Christensen and Mooney*, 1995].

straight line. This procedure enables to carry out a 2-D model but implies errors that are most important when the structures are not strictly perpendicular to the acquisition and projection line. In those cases, stations lying into a particular lithology maybe projected onto a different one. Other contributions to traveltime mismatches include the topography along the line. Note that there is a 600 m variation in the altitudes along the profile, with local oscillations (short wavelength, on the order of 10 km) that go from tens to 150 m, caused by the different outcropping lithologies or the structures. These altitude variations produce traveltime errors that may get up to 0.05 s, assuming a *P* wave velocity of 3 km/s. Near-surface velocity variations can also add up errors in the modeled traveltimes. However, the weathering layer is very thin and most of the surface outcrops are characterized by relatively high velocities, which decrease the static shifts to values of around 0.01 s. Errors due to lack of consistency/homogeneity during the traveltime picking procedure is another source of error. This source of error is very dependent on the predominant frequencies of the arrivals, being larger at the lower frequencies. Phases with frequencies around 4–5 Hz, and an average velocity of 4000 m/s, lead to picking traveltime uncertainties of 0.05 s. The considered mismatches may account for velocity errors ranges between 0.1 and 0.2 km/s and depth uncertainties on the order of 0.4 km, which is considered to be nonrelevant for the interpretation of the model.

Lateral resolution is constrained by the length of the identified phases and by that of the areas sampled by rays sampling each interface. Figure 6 shows the phases picked in every shot record, revealing that energy is sometimes followed from normal incidence (0 km offset) to offsets above 150 km. Long Pg and PmP phases are observed throughout the experiment, thus providing good constraints on the geometry of the interfaces at long offsets. Figure 7b shows the range of distances in which each interface is sampled. Note that the geometry and depth of the Moho and the crustal average velocities are controlled along most of the profile. Only the southernmost 40 km lacks the information provided by incident rays (Figure 7b).

4. Bouguer Anomaly Gravity Constraints

The 2-D projection of the Bouguer gravity anomaly (Figure 3) along a 30 km wide strip centered at the seismic transect varies from slightly positive values (10 mGal) to the south, in the CU area, to strongly negative values (−120 mGal) to the north (Figure 8c). Note that, along the profile, the average topography is relatively high, centered at, approximately, 600–700 m (Figure 8c). A qualitative analysis suggests that the regional trend of the anomaly is indicative of an increase in crustal thickness to the north. The displayed overall variability of the measurements which is revealed by the standard deviation of the projected values (Figure 8c) is relatively low, except in the areas corresponding to the Los Pedroches and Mora Batholiths. Here the existence of elongated granitic bodies, although perpendicular to the transect, hinders the 2-D assumption and increases the variability of the anomaly. Nevertheless, the good knowledge of surface geology assures the reliability of the model.

In order to study the compatibility of the *P* wave velocity model with the observed Bouguer gravity anomaly [*Ayala*, 2013], the velocity model was converted to densities using the empirical relations by *Brocher* [2005]. This formulation is applicable to most lithologies, although caution must be used when working with mafic and calcium-rich rocks. Specific average densities for the shallowest features include values of 2520 kg/cm^3 for the "Los Pedroches" Batholith area and of 2300 kg/m^3 for the sediments within the TB. A density range from 2600 kg/m^3 to 2670 kg/m^3 is calculated for the uppermost crust down to ~5 km depth (Table 3). The rest of the upper crust is characterized by a density range from 2800 kg/m^3 in the north to 2750 kg/m^3 in the south (Figure 8d). The mid-lower crust has a constant density of 2950 kg/m^3. For the uppermost lithospheric mantle, the density is 3300 kg/m^3. Overall, the observed and calculated gravity anomalies are in relatively good agreement (Figure 8c). The most important feature of the gravity model is the northward increase in the crustal thickness and density. This feature, already identified in the *P* wave velocity model, contrasts with the constant traveltime (twtt) at which the Moho is observed in the vertical incidence section. The gravity model shows how the increase in the crustal velocities to the north needs to be compensated by an increase in crustal densities and by the deepening of the Moho (increase in crustal thickness). This reflects in the decrease of the long-wavelength Bouguer gravity anomaly illustrated in Figure 8c.

Regarding the short wavelength components of the anomaly, the slightly positive values at the southern end of the transect can be associated to the suture zone (the CU: high-grade metamorphics with slices of

Table 3. Corresponding Rock Types for the Temperature-Corrected *P* Wave Velocities and Densities[a]

Depth (km)	Velocity (km/s)	Density (kg/m^3)	Rock Types
0–5	3.3–4.0	2300	Cenozoic sediments granite and granodiorite (Pedroches batholith), slate and greywacke[h]
	5.2–5.6	2520	
	5.4–5.8	2600–2670	metasedimentary rocks: slate, greywacke, schist, gneiss, sandstone, limestone, quartzite[h]
	-	2900	interbedded thin layers of basalts[h]
5–20	5.8–6.6	2750–2800	slate, diorite, granodiorite, gneiss, felsic granulite[e]; greywacke[b]
20–32	6.6–7.2	2850–2950	amphibolite, diabase, mafic granulite, gabbro norite[e]; kyenite schist[c]; gneiss[f]
32–50	7.2–8.2	3300	mixture of mafics and ultramafics (lherzolite, harzburgite[(d,g)]; pyroxenite, dunite, peridotite[e]; eclogite [d,g]) with a dominant composition of pyroxenite

[a]Data modified from *Hawman et al.* [1990].
[b]*Birch* [1960].
[c]*Christensen* [1965].
[d]*Carmichael* [1989].
[e]*Christensen and Mooney* [1995].
[f]*Rudnick and Fountain* [1995].
[g]*Kern et al.* [1999].
[h]*García-Lobón et al.* [2014].

mafic rocks) and Variscan mafic igneous rocks in that area. The minimum observed at 60 km is related to the Los Pedroches batholith. Finally, the minimum values observed to the northern end of the transect are related to the low-density sediments of the TB. Even though the basin-scale wavelength of the anomaly is explained by the basin itself, the smooth northward decrease in the gravity anomaly reflects changes already constrained by the *P* wave velocity model: smooth increase in crustal thickness and an increase in seismic velocities (and densities) toward the northern end of the transect.

5. Discussion

5.1. Constraints of the *P* Wave Velocity Model on the Lithology

The composition and nature of the subsurface rocks may be constrained by the *P* wave velocities and the derived density model (Figures 8b and 8d). Laboratory measurements of seismic velocities at high temperature and confining pressures on different crustal rock types [e.g., *Carmichael*, 1989; *Christensen and Mooney*, 1995] may be compared with our *P* wave velocity model in order to get hints about the lithologies conforming the subsurface. As thermal gradients and pressure have an influence on the *P* wave velocity of rocks [*Kern*, 1978; *Christensen and Salisbury*, 1979; *Kern and Richter*, 1981], laboratory velocity measurements used in this paper are corrected for the effect of temperature using a geotherm of 20° C/km, assumed to exist in the region, not too different from the one proposed to the south by *Marzan* [2000] and used by *Palomeras et al.* [2011b]. A large number of common crustal rock types have similar *P* wave velocity [*Christensen and Mooney*, 1995], so density values will be used to partly decrease the uncertainties (Table 3).

P wave velocities are laterally variable in the upper crust and feature velocities within the range of 5.2 km/s to 6.6 km/s (Figure 8b). To the south of shot A4, the upper crust can be divided into two layers: a near-surface layer, ~5 km thick, reveals a velocity gradient from 5.2 km/s to 5.6 km/s. The resulting densities (Figure 8d) range from 2520 kg/m^3 to 2670 kg/m^3. To the north, the TB is characterized by velocities of 3.3 km/s to 4.0 km/s and an average density of 2300 kg/m3. Within the CU, the CIZ and the TB, the outcropping lithologies (Figures 2a, 2b, and 8a) are consistent with the velocities and densities of the proposed model. The most compatible rocks in the uppermost crust for these velocities and densities include: granite, granodiorite, slate, greywacke, schist, gneiss, sandstone, limestone, and quartzite, most of them outcropping along the section.

Underneath the near-surface layer, velocities increase from 5.6 km/s up to 6.2 km/s at 13–20 km depth. In the model, the corresponding density ranges from 2750 kg/m^3 to 2800 kg/m^3 for this layer (Figure 8d). However, below the TB, *P* wave velocities vary from 6.0 km/s to 6.4 km/s at 15–20 km depth implying higher velocities with a, however, smoother gradient. These higher velocities can be explained by the presence of igneous rocks of acidic or intermediate character and/or to lithologies with a higher degree of metamorphism. The compatible rocks for this specific layer include slate, diorite, granodiorite, gneiss, felsic granulite, and greywacke [*Birch*, 1960; *Christensen and Mooney*, 1995] and may correspond to a high-grade/igneous Variscan or pre-Variscan basement. To the north, some of these lithologies are observed in local outcrops.

The velocities and density values within the mid-lower crust, from 13 to 20 km depth to the Moho, are more homogeneous and perform small lateral changes (Figures 8b and 8d). This shows that the CIZ represent a unique precollisional terrane and that its Variscan orogenic evolution implies marked differences only at upper crustal levels. The fact that the mid-lower crust is slightly thinner to the north (Figure 8b) may be related to the existence of partial melt processes acting as differentiating mechanisms across the crust in this area. The ALCUDIA-NI image [*Martínez Poyatos et al*., 2012, Figure 7; *Ehsan et al.,* 2014, Figure 9] also shows the thinner mid-lower crust to the north. The tectonic interpretation of the mid-lower crustal thinning toward the north is associated with a ramp structure [*Martínez Poyatos et al*., 2012; *Ehsan et al.,* 2014]. The upper part of the mid-lower crust shows a velocity of 6.8 km/s and a density value of 2850 kg/m^3 at 20–23 km depths. From ~20 km depth down to the Moho, it features a smooth velocity gradient from 6.6–6.8 km/s to 7.2 km/s. A constant density of 2950 kg/m^3 for the entire layer is a good representation of the *P* wave velocities obtained for this layer. The rock types that are consistent with these velocities and the computed densities include amphibolite, diabase, mafic granulite, gabbro norite, kyenite schist, and gneiss [*Christensen*, 1965; *Christensen and Mooney*, 1995; *Rudnick and Fountain*, 1995]. The upper mantle presents *P* wave velocities around 8.0 km/s and a density of 3300 kg/m^3. Consistent rock types are likely a mixture of mafics and ultramafics rocks (lherzolite, harzburgite, pyroxenite, dunite, peridotite, and eclogite) [*Carmichael*, 1989; *Christensen and Mooney*, 1995; *Kern et al.,* 1999]. The *P* wave velocity model (Figure 8b) is gradual from the Moho to depths of 50 km, with a velocity range of 8.0 km/s to 8.4 km/s. However, we have no control of the *P* wave velocity gradient below 40–42 km (Figure 8b); and therefore, we cannot extract any conclusions about the composition. However, the most probable rock types interpreted at those depths include dunite, eclogite, and peridotite [*Carmichael*, 1989].

The crustal composition inferred for the ALCUDIA-WA section would be greatly improved by the study of *S* waves and the calculation of Poisson's ratios. This parameter is sensible to the amount of quartz in the rocks and can establish differences between different types of igneous rocks and crustal compositions. This subject will be one of the scopes of future works to carry on with this good quality data set. Although the model presented here agrees with all the geophysical observables acquired up to date, the recognition of specific structures, processes, and lithologies is still subject to considerable ambiguity. These issues can only be unraveled with the assistance of additional geophysical information, especially with the acquisition of deep multiseismic reflection data in the CS and the northern part of the CIZ.

5.2. The Crust Beneath the Central Iberian Zone

The derived *P* wave velocity model (Figure 8b) from wide-angle seismic reflection data reveals the presence of two crustal scale discontinuities. The first one, located approximately at 13 km depth to the south and 20 km depth to the north, is defined as a midcrustal discontinuity. The second one, the crust-mantle discontinuity or Moho is located at 31 km depth to the south and 35.5 km to the north. The first interface most probably represents the brittle/ductile transition, because of its depth and because of the seismic fabrics it bounds. An intracrustal phase (PiP) is observed in all shot gathers (Figures 6a–6d) along the main transect. This PiP phase placed strong constraints on the boundary between the upper and mid-lower crust. The high-amplitude *P* wave reflected at the Moho discontinuity, the PmP phase, identified in the shot gathers (Figures 6a–6d) constrains the crustal thickness beneath the CIZ and the TB.

The *P* wave velocity model (Figure 8b) reveals a relatively sharp velocity transition from 6.2 km/s to 6.6 km/s capable of producing the moderately reflective PiP events. The velocity contrast across this interface is less prominent toward the northern part of the profile, which might respond for the little reflectivity this event shows in the northern part of shot A3. Where the wavelet identified as corresponding to this interface features higher frequencies, a coda is observed suggesting interface changes in the internal structure and/or the transition to a very reflective lower crust (Figure 4), i.e., a layered sequence of low- and high-velocity lithologies. The velocity contrast would be relatively small; however, the layering should be within one fourth of the predominant wavelength of the seismic wavelet so that constructive interference should be possible.

In the nearly coincident ALCUDIA-NI deep seismic reflection transect (Figures 2 and 3), a similar interface was depicted on top of the very reflective and laminated mid-lower crust [*Martínez Poyatos et al*., 2012, Figure 4; *Ehsan et al.,* 2014, Figure 4]. There, the reflection fabric changes from high dips in the upper crust to almost horizontal and probably boudinaged in the lower crust. This transect was divided in three segments depending on the seismic reflection fabric and structures identified mainly in the lower crust

[*Martínez Poyatos et al*., 2012, Figure 4; *Ehsan et al.,* 2014, Figure 4]. Although Variscan shortening is homogeneously distributed in the upper crust [*Martínez Poyatos et al*., 2012; *Ehsan et al.,* 2014], the mid-lower crust of the southern and northern segments is relatively more deformed than the central segment [*Martínez Poyatos et al*., 2012; *Ehsan et al.,* 2014]. In the central segment, the upper crust features synclinal and anticlinal geological structures cored by the blind thrusts, whereas no shortening structures are identified in the mid-lower crust [*Martínez Poyatos et al*., 2012; *Ehsan et al.,* 2014]. The shortening is concentrated mainly in lower crust of the southern and central segments [*Martínez Poyatos et al*., 2012; *Ehsan et al.,* 2014]. The ALCUDIA-NI transect shows that the upper and mid-lower crust reacted differently to shortening in different segments, thus a decoupling zone (corresponding to the brittle/ductile transition) was defined at ~13 km depth which separated the upper crust from the mid-lower crust [*Martínez Poyatos et al*., 2012]. The results from experiments on shortening of layered analogue models [*Davy and Cobbold*, 1991; *Burg et al.,* 1994; *Brun*, 2002] that incorporate the brittle/ductile rheological stratification of crustal materials reveal similar features. The localized and/or distributed deformation is largely controlled by the coupling/decoupling between brittle and ductile layers [*Brun*, 2002]. Similarly, in the IBERSEIS transects [*Simancas et al.,* 2003, Figure 3; *Palomeras et al.,* 2009, 2011a, Figures 5, 6 8, and 9] acquired to the southwest of the study area (Figure 1) a midcrustal discontinuity was also identified to be at 13–14 km depth. In the latter, the fault associated structures imaged in the upper crust and the high reflectivity shear zones observed in the lower crust had opposing dips, flattening out at that midcrustal boundary [*Simancas et al.,* 2003, Figure 3].

The second major interface is found at the base of the crust. The Moho boundary generates very high amplitude reflections from near vertical (0 km) offsets to over 200 km offset (Figure 6). A sharp velocity increase is modeled across this interface, from 7.1–7.2 km/s to values around 8.0 km/s, thus producing a high-amplitude and relatively high frequency reflection, the PmP. Pn is imaged as a first arrival for offsets in excess of 120–135 km. For reduction velocities of 8.0 km/s, it dips to the near offsets when the waves are traveling southward (updip) and is nearly horizontal when the waves travel north (downdip), suggesting again the existence of another north dipping boundary: the Moho. Accordingly, the velocity model reveals significant differences in the depth position of this interface between the southern and northern end of the profile. In the south, the crust-mantle boundary is located at 31 km, while to the north this interface is located at 35.5 km depth. Finally, the first arrival (Pg) evidences an increase in the velocities of the upper crust in the CIZ from south (at the CU) to the north (at the southern boundary of the CS). These lateral variations in the crustal thickness and physical properties have not been reported previously and constitute the most significant results of the analysis and interpretation of the ALCUDIA-WA seismic reflection data set.

Similar to other multiseismic studies developed by Lithoprobe in Canada across the Trans-Hudson orogen [*Németh et al.,* 2005] and/or the normal incidence and wide-angle seismic reflection data acquired across the southern Ural Mountains [*Berzin et al.,* 1996; *Carbonell et al.,* 1996, 2002], in the ALCUDIA sections there is a correlation between structures mapped by both types of seismic data sets. However, the normal incidence seismic reflection profile [*Martínez Poyatos et al*., 2012; *Ehsan et al.,* 2014] and the overlapping gravity study [*García-Lobón et al.,* 2014] did not reveal a significant variation in crustal thickness from south to north. The ALCUDIA-NI profile is ~65 km shorter than the ALCUDIA-WA profile, and it does not reach the TB and the southernmost boundary of the CS (Figures 2b and 3). Furthermore, no detailed wide-angle crustal velocity information was available before the current study so that reliable time to depth conversion could not be attempted. Once the time-migrated stack of the normal incidence profile is converted to depth using the wide-angle velocities, a coincidence in the Moho images is resolved (Figure 8e). However, prestack depth migration should be carried out using the calculated *P* wave crustal velocities in order to assess the accurate depths of the crustal boundaries. The normal incidence section [*Martínez Poyatos et al*., 2012, Figure 4; *Ehsan et al.,* 2014, Figure 4] reveals a high-amplitude reflective fabric to the south at 13–15 km depth, depicting a break between the poorly reflective upper crust and the laminated lower crust (Figure 8e). This boundary approximately coincides with the proposed brittle-ductile transition constrained by the wide-angle data. On the other hand, a Moho event that dips into the mantle at 60 km from the southern end of the line is not imaged by the wide-angle data (Figure 8b). Further to the north and near the location of shot A4 (~200 km), the normal incidence data reveal a clear pinch-out at 20 km depth [*Martínez Poyatos et al*., 2012, Figure 7; *Ehsan et al.,* 2014, Figure 9] interpreted as a ramp structure. This is related to a geometrically similar velocity/density anomaly detected from wide-angle and gravity modeling (Figures 8d and 8e). Finally, the

poorly reflective boundary observed in the vertical incidence data and interpreted as the brittle-ductile transition is located at around 20 km in its northern end, which again overlaps the interface between the upper and mid-lower crust as deduced in the *P* wave velocity model.

The crustal model (Figure 8b) obtained for the CIZ on the basis of the ALCUDIA-WA profile differs from that obtained for the southernmost CIZ using the IBERSEIS wide-angle seismic reflection data set (Figures 5 and 6) [*Palomeras et al.,* 2011a]. The latter was acquired to the southwest of the ALCUDIA experiment and even though they structurally overlap in a section that extends 100 km to the north of the CU into the CIZ, the velocity structure is different. The IBERSEIS data set samples an area where a high-velocity midcrustal body, the IRB, has been identified [*Simancas et al.,* 2003, Figure 3]. The size (175 km long) and physical properties of this laccolith-type intrusion determine some variations in the crustal thickness. The high velocities at midcrustal levels suggest the presence of mafic mantle-derived rocks [*Palomeras et al.,* 2009, 2011a]. In the IBERSEIS-A section, crustal thickness in the CU area is around 35 km [*Palomeras et al.,* 2011a, Figure 5]. Section B, located to the east of section A [*Palomeras et al.,* 2011a, Figure 6], and closer to the ALCUDIA-WA profile, already shows a shallower Moho in the CU (33–34 km). In both cases, this interface shallows to the north getting to 31–32 km, the same values as those estimated by the ALCUDIA-WA profile (Figure 8b). Apart from this local difference, both experiments get similar results regarding overall crustal velocities (excluding the IRB) and crustal thickness of the southern CIZ. Together, they provide a 600 km long structural and velocity model of the SW Iberian Massif.

5.3. Origin of the Crustal Thickening/Moho Deepening

The distribution of velocities derived from the 2-D velocity model (Figures 8b and 8f) across two sections (one to the south and a northern one) from the ALCUDIA-WA seismic reflection profile are compared with standard velocity-depth functions for different types of crust [*Christensen and Mooney*, 1995]. The velocity-depth function (Figure 8f) to the south of shot A4 features relatively lower velocity values for the upper crust (blue box in Figure 8b) than those obtained to the north of shot A4 (black box in Figure 8b). Even though the velocities in the upper crust from both profiles differ, they match those found on average continental crust. However, at middeep crustal levels, velocities are close to those found in rifts and extended crust [*Christensen and Mooney*, 1995], suggesting the existence of extensional and melting processes affecting the crust, which have been already described to the north, near the CS. Note that the lower crust appears to have similar average velocities in both cases (Figures 8b and 8f). Note also that the average topography (Figure 8c) stays at nearly the same level of 600–700 m except for limited local variations due to contrasting lithologies at surface. These lateral velocity changes are accompanied by density changes (Figure 8d) and evidence a northward variation of lithologies and probably different tectonic evolution.

To the north of the study area, the CS (Figure 1) represents one of the most internal domains of the Iberian Variscan Orogen. Here Variscan crustal thickening has been important and has led to partial melting and to the production of voluminous igneous rocks [*Rubio Pascual et al.,* 2013; *Simancas et al.,* 2013]. Regardless of the processes involved in crustal thickening, it is clear that rocks occupying shallow crustal levels to the north are denser than those outcropping to the south and have their origin in deeper structural levels. Neoproterozoic to Early-Cambrian metasediments, migmatitic and mylonitic Early Ordovician orthogneisses outcrop in the vicinity of shot A5 and are expected at shallow depths elsewhere. There, omphacite and rutile inclusions in garnet have been related to earlier, midtemperature eclogite facies conditions of ≈ 1.4 GPa and 725–775°C [*Barbero and Villaseca*, 2000; *Villaseca et al.,* 2014], thus indicating a deep precedence of some near-surface rocks. This increase in density/velocity at shallow crustal depths needs an increase in crustal thickness to explain the Bouguer gravity anomaly. The origin of this thickening might be related to the alpine tectonics affecting the area and to the orogenic load associated to the CS mountain range. However, if we consider the little change in altitude along the profile, the Moho deepening may also be related to the isostatic response of the crust to denser lithologies. Further seismic investigations to the north, across the CS, are necessary in order to address if crustal thickening/Moho deepening continues to the north and if it is related to high topographies and to the alpine tectonics.

6. Conclusions

Traveltime interpretation of the ALCUDIA-WA profile acquired over the CIZ has led to a well-constrained, approximately 280 km long and 50 km deep, *P* wave seismic velocity model. The high-resolution shot gathers

feature clear *P* wave reflections and refractions at all crustal levels that can be correlated from shot to shot. The velocity-depth model reveals a layered velocity structure though prominent lateral velocity variations that are evident in the upper crust down to ~15 km depth beneath the TB. The velocity model can be divided into two segments according to the velocity isolines traced for the upper crust: (a) the southern part, sampling the CU and the southern CIZ and (b) the northern part, from the Toledo Anatectic Complex to the TB. On average, the velocities for the upper crust within the CU and the CIZ range from 5.2 km/s in the surface to 6.2 km/s in the boundary with the mid-lower crust. Below the TB, *P* wave velocities range from 5.4 km/s to more than 6.4 km/s revealing a significant lateral gradient that reflects the presence of high-grade metamorphic rocks and/or acidic to intermediate igneous rocks near the surface. The average density for the upper crust is within the range of 2300 kg/m^3 in the surface to 2800 kg/m^3 at 13–20 km depth. The boundary between the upper and mid-lower crust is characterized by a velocity contrast from 6.2 km/s to 6.6 km/s in the south and 6.4 km/s to 6.6 km/s to the north. The velocity contrast between the upper and mid-lower crust is not significant to the north. The *P* wave velocities within the mid-lower crust are more homogeneous along the entire profile, ranging from 6.6 km/s to 7.2 km/s. The density within the mid-lower crust shows a range of 2850 kg/m^3 to 2950 kg/m^3. The crust-mantle transition features a sharp *P* wave velocity contrast from 7.2 km/s to 8.0 km/s that constrains the Moho across the CIZ.

High-amplitude PiP and PmP phases suggest the existence of two major discontinuities: the brittle/ductile discontinuity at ~13–20 km and Moho boundary at ~31–35.5 km, from south to north. Both of them are interpreted to act as decoupling zones and represent levels of lithological/rheological variations. The velocity-depth functions for the CIZ show that velocities in the upper crust match with those found in typical average continental crust. However, the mid-lower crustal velocities fit those found in rifts and extended crust. The presence of extensional tectonics indicates intrusions of possible mantle-derived magmas and that melting processes affect in the crust. The increase in Moho depth along the CIZ is associated to higher *P* wave velocity values and correlates with changes in lithology in the outcropping geology. This is most probably a result of the different tectonic evolution affecting at the most internal parts of this tectonic zone of the Iberian Variscan transpressive belt. In this area, right to the south of the CS mountain range, Variscan crustal thickening resulted in generalized remobilization and partial melt, producing igneous rocks and taking structurally deep, denser, and faster rocks to shallower crustal levels. Factors contributing to the Moho deepening and/or crustal thickening may be the crustal isostatic response to denser lithologies, the orogenic load associated to the CS, and the tectonics associated to the Alpine orogeny.

Acknowledgments

Seismic data were collected in 2012 with funding provided by the Spanish Ministry of Science and Innovation (grants CGL2004-04623/BTE, CGL2007-63101/BTE, CGL2011-24101, and CSD2006-00041). Instrumentation was provided by the IRIS-PASSCAL instrument center, Socorro, New Mexico, USA. S.A. Ehsan is funded by the European Commission grant Marie Curie Actions (264517-TOPOMOD-FP7-PEOPLE-2010-ITN). We thank Instituto Geológico y Minero de España for providing the logistic help and an academic crew for data acquisition. We gratefully acknowledge the constructive comments and suggestions from Tanya Fomin and two anonymous reviewers. Marcel Cembrowski, Ignacio Marzan, Dennis Brown, and Giovanni Camanni are acknowledged for the valuable suggestions related to data interpretation. GMT was used to prepare some of the figures shown in the paper.

References

Artemieva, I. (2007), Dynamic topography of the East European craton: Shedding light upon lithospheric structure, composition and mantle dynamics, *Global Planet. Change*, *58*(1–4), 411–434.

Ayala, C. (2013), A new compilation of gravity data over the Iberian Peninsula and surrounding areas, Internal Report Topolberia project (Consolider-Ingenio), 20 pp., IGME.

Ayarza, P., J. R. Martínez Catalán, J. Gallart, J. A. Pulgar, and J. J. Dañobeitia (1998), Estudio Sísmico de la Corteza Ibérica Norte 3.3: A seismic image of the Variscan crust in the hinterland of the NW Iberian Massif, *Tectonics*, *17*, 171–186, doi:10.1029/97TC03411.

Ayarza, P., J. R. Martínez Catalán, J. Alvarez-Marrón, H. Zeyen, and C. Juhlin (2004), Geophysical constraints on the deep structure of a limited ocean-continent subduction zone at the North Iberian Margin, *Tectonics*, *23*, TC1010, doi:10.1029/2002TC001487.

Ayarza, P., I. Palomeras, R. Carbonell, J. C. Afonso, and J. F. Simancas (2010), A wide-angle upper mantle reflector in SW Iberia: Some constraints on its nature, *Phys. Earth Planet. Inter.*, *181*, 88–102, doi:10.1016/j.pepi.2010.05.004.

Azor, A., F. González Lodeiro, and J. F. Simancas (1994), Tectonic evolution of the boundary between the Central Iberian and Ossa-Morena zones (Variscan Belt, SW Spain), *Tectonics*, *13*, 45–61, doi:10.1029/93TC02724.

Barbero, L., and C. Villaseca (2000), Eclogite facies relics in metabasites from the Sierra de Guadarrama (Spanish Central System) P–T estimations and implications for the Hercynian evolution, *Min. Mag.*, *64*, 815–836.

Berzin, R., O. Oncken, J. H. Knapp, A. Pérez-Estaún, T. Hismatulin, N. Yunusov, and A. Lipilin (1996), Orogenic evolution of the Ural Mountains: Results from an integrated seismic experiment, *Science*, *274*(5285), 220–221, doi:10.1126/science.274.5285.220.

Birch, F. (1960), The velocity of compressional waves in rocks to 10 kilobars, *J. Geophys. Res.*, *65*, 1083–1102, doi:10.1029/JZ065i004p01083.

Brocher, T. M. (2005), Empirical relations between elastic wave speeds and density in the Earth's crust, *Bull. Seismol. Soc. Am.*, *95*, 2081–2092.

Brun, J.-P. (2002), Deformation of the continental lithosphere: Insights from brittle-ductile models, in *Deformation Mechanisms, Rheology and Tectonics: Current Status and Future Perspectives*, edited by S. De Meer et al., *Geol. Soc. London Spec. Publ.*, *200*, 355–370.

Burg, J.-P., M. Iglesias, P. Laurent, P. Matte, and A. Ribeiro (1981), Variscan intracontinental deformation: The Coimbra-Córdoba shear zone (SW Iberian Peninsula), *Tectonophysics*, *78*, 161–177, doi:10.1016/0040-1951(81)90012-3.

Burg, J.-P., P. Davy, and J. Martinod (1994), Shortening of analogue models of the continental lithosphere: New hypothesis for the formation of the Tibetan plateau, *Tectonics*, *13*, 475–483, doi:10.1029/93TC02738.

Carbonell, R. (2004), On the nature of mantle heterogeneities and discontinuities: Evidence from a very dense wide-angle shot record, *Tectonophysics*, *388*(1–4), 103–117, doi:10.1016/j.tecto.2004.07.025.

Carbonell, R., and TOPOIBERIA WG (2006), New research initiatives for imaging the Iberian lithosphere, Abstract T43C-1648 presented at 2006 Fall Meeting, AGU.

Carbonell, R., A. Pérez-Estaún, J. Gallard, J. Díaz, S. Kasubin, J. Mechie, R. Stadtlander, A. Schulze, J. H. Knapp, and A. Morozov (1996), Crustal root beneath the Urals: Wide-angle seismic evidence, *Science*, *274*(5285), 222–224, doi:10.1126/science.274.5285.222.

Carbonell, R., D. Lecerf, M. Itzin, J. Gallart, and D. Brown (1998), Mapping the Moho beneath the southern Urals with wide-angle reflections, *Geophys. Res. Lett.*, *25*, 4229–4232, doi:10.1029/1998GL900107.

Carbonell, R., J. Gallart, A. Pérez-Estaún, J. Díaz, S. Kashubin, J. Mechie, F. Wenzel, and J. Knapp (2000), Seismic wide-angle constraints on the crust of the southern Urals, *J. Geophys. Res.*, *105*, 13,755–13,777, doi:10.1029/2000JB900048.

Carbonell, R., J. Gallart, and A. Pérez-Estaún (2002), Modelling and imaging the Moho transition: The case of the southern Urals, *Geophys. J. Int.*, *149*(1), 134–148, doi:10.1046/j.1365-246X.2002.01623.x.

Carbonell, R., F. Simancas, C. Juhlin, J. Pous, A. Pérez-Estaún, F. González-Lodeiro, G. Muñoz, W. Heise, and P. Ayarza (2004), Geophysical evidence of a mantle derived intrusion in SW Iberia, *Geophys. Res. Lett.*, *31*, L11601, doi:10.1029/2004GL019684.

Carmichael, R. S. (1989), *Physical Properties of Rocks and Minerals*, CRC Press, Boca Raton, Fla.

Christensen, N. (1965), Compressional wave velocities in metamorphic rocks at pressures to 10 kilobars, *J. Geophys. Res.*, *70*, 6147–6164, doi:10.1029/JZ070i024p06147.

Christensen, N., and N. Salisbury (1979), Seismic anisotropy in the oceanic upper mantle: Evidence from the Bay of Islands Ophiolite Complex, Newfoundland, *J. Geophys. Res.*, *70*, 4601–4610, doi:10.1029/JB084iB09p04601.

Christensen, N. I., and W. D. Mooney (1995), Seismic velocity structure and composition of the continental crust: A global view, *J. Geophys. Res.*, *100*(B6), 9761–9788, doi:10.1029/95JB00259.

Cloetingh, P. A., et al. (2007), TOPO-EUROPE: The geoscience of coupled deep Earth-surface processes, *Global Planet. Change*, *58*(1–4), 1–118, doi:10.1016/j.gloplacha.2007.02.008.

Cloetingh, S., J. Gallart, G. de Vicente, and L. Matenco (2011), TOPO-EUROPE: From Iberia to the Carpathians and analogues, *Tectonophysics*, *502*(1–2), 1–27, doi:10.1016/j.tecto.2010.11.008.

Cook, F. A., A. J. van der Velden, and K. W. Hall (1999), Frozen subduction in Canada's Northwest Territories: Lithoprobe deep lithospheric reflection profiling of the western Canadian Shield, *Tectonics*, *18*, 1–24, doi:10.1029/1998TC900016.

Cook, F. A., D. J. White, A. G. Jones, D. W. S. Eaton, J. Hall, and R. M. Clowes (2010), How the crust meets the mantle: Lithoprobe perspectives on the Mohorovicic discontinuity and crust-mantle transition, *Can. J. Earth Sci.*, *47*, 315–351, doi:10.1139/E09-076.

Davy, P., and P. Cobbold (1991), Experiments on shortening of a 4-layer model of the continental lithosphere, *Tectonophysics*, *188*, 1–25, doi:10.1016/0040-1951(91)90311-F.

de Vicente, G., and A. Muñoz-Martín (2013), The Madrid Basin and the Central System: A tectonostratigraphic analysis from 2D seismic lines, *Tectonophysics*, *602*, 259–285.

Ehsan, S. A., R. Carbonell, P. Ayarza, D. Martí, A. Pérez-Estaún, D. J. Martínez-Poyatos, J. F. Simancas, A. Azor, and L. Mansilla (2014), Crustal deformation styles along the reprocessed deep seismic reflection transect of the Central Iberian Zone (Iberian Peninsula), *Tectonophysics*, *621*, 159–174, doi:10.1016/j.tecto.2014.02.014.

Flecha, I., I. Palomeras, R. Carbonell, F. Simancas, P. Ayarza, J. Matas, F. González-Lodeiro, and A. Peréz-Estaún (2009), Seismic imaging and modelling of the lithosphere of SW-Iberia, *Tectonophysics*, *472*(1–4), 148–157, doi:10.1016/j.tecto.2008.05.033.

Franke, W. (2000), The mid-European segment of the Variscides: tectonostratigraphic units, terrane boundaries and plate tectonic evolution, in *Orogenic Processes: Quantification and Modelling in the Variscan Belt*, edited by W. Franke et al., *Geol. Soc. London Spec. Publ.*, *179*, 35–61, doi:10.1144/GSL.SP.2000.179.01.05.

Freeman, B., S. L. Klemperer, and R. W. Hobbs (1988), The deep structure of the northern England and the Iapetus suture zone from BIRPS deep seismic reflection profiling, *J. Geol. Soc.*, *145*, 727–740, doi:10.1144/gsjgs.145.5.0727.

García-Lobón, J. L., C. Rey-Moral, C. Ayala, L. M. Martín-Parra, J. Matas, and M. I. Reguera (2014), Regional structure of the southern segment of Central Iberian Zone (Spanish Variscan Belt) interpreted from potential field images and 2.5 D modelling of Alcudia gravity transect, *Tectonophysics*, *614*, 185–202, doi:10.1016/j.tecto.2013.12.005.

Hawman, R. B., R. H. Colburn, D. A. Walker, and S. B. Smithson (1990), Processing and inversion of refraction and wide-angle reflection data from the 1986 Nevada Passcal Experiment, *J. Geophys. Res.*, *95*, 4657–4691, doi:10.1029/JB095iB04p04657.

Hinze, W. J., et al. (2005), New standards for reducing gravity data: The North American gravity database, *Geophysics*, *70*, J25–J32.

Kern, H. (1978), The effect of high temperature and high confining pressure on compressional wave velocities in quartz-bearing and quartz-free igneous and metamorphic rocks, *Tectonophysics*, *44*, 185–203, doi:10.1016/0040-1951(78)90070-7.

Kern, H., and A. Richter (1981), Temperature derivatives of compressional and shear wave velocities in crustal and mantle rocks at 6 k bar confining pressure, *J. Geophys.*, *49*(1–4), 47–56.

Kern, H., S. Gau, Z. Jin, T. Popp, and S. Jin (1999), Petrological studies on rocks from the Dabie ultrahigh pressure (UHP) metamorphic belt, central China: Implications for the composition of the lower crust, *Tectonophysics*, *301*, 191–215, doi:10.1016/S0040-1951(98)00268-6.

Klemperer, S. L., and D. H. Matthews (1987), Iapetus suture located beneath the North Sea by BIRPS deep seismic reflection profiling, *Geology*, *15*, 195–198, doi:10.1130/0091-7613(1987)15<195:ISLBTN>2.0.CO;2.

Martínez Catalán, J. R., D. Martínez Poyatos, and F. Bea (2004), Zona Centroibérica: Introducción, in *Geología de España*, edited by J. A. Vera, pp. 68–69, Soc. Geol. Esp.-Inst. Geol. Min. Esp., Madrid.

Martínez Poyatos, D., et al. (2012), Imaging the crustal structure of the Central Iberian Zone (Variscan Belt): The ALCUDIA deep seismic reflection transect, *Tectonics*, *31*, TC3017, doi:10.1029/2011TC002995.

Marzan, I. (2000), Régimen térmico en la Península Ibérica. Estructura litosférica a través del Macizo Ibérico y el Margen Subportuges, PhD thesis, Barcelona Univ., Spain.

Matte, P. (1986), Tectonics and plate tectonics model for the Variscan Belt of Europe, *Tectonophysics*, *126*, 329–374, doi:10.1016/0040-1951(86)90237-4.

Matte, P. (2001), The Variscan collage and orogeny (480–290 Ma) and the tectonic definition of the Amorica microplate: A review, *Terra Nova*, *13*, 122–128, doi:10.1046/j.1365-3121.2001.00327.x.

Németh, B., R. Clowes, and Z. Hajnal (2005), Lithospheric structure of the Trans-Hudson orogen from seismic refraction—Wide-angle reflection studies, *Can. J. Earth Sci.*, *42*(4), 435–456, doi:10.1139/e05-032.

Onken, O., A. Plesh, J. Weber, W. Ricken, and S. Schrader (2000), Passive margin detachment during arc-continent collision (central European Variscides), in *Orogenic Processes: Quantification and Modelling in the Variscan Belt*, edited by W. Franke et al., *Geol. Soc. London Spec. Publ.*, *179*, 9–20.

Palomeras, I., R. Carbonell, I. Flecha, F. Simancas, P. Ayarza, J. Matas, D. Martinez Poyatos, A. Azor, F. González Lodeiro, and A. Pérez-Estaún (2009), The nature of the lithosphere across the Variscan orogen of SW-Iberia: Dense wide-angle seismic reflection data, *J. Geophys. Res.*, *114*, B02302, doi:10.1029/2007JB005050.

Palomeras, I., R. Carbonell, P. Ayarza, D. Martí, D. Brown, and J. F. Simancas (2011a), Shear wave modeling and Poisson's ratio in the Variscan Belt of SW Iberia, *Geochem. Geophys. Geosyst.*, *12*, Q07008, doi:10.1029/2011GC003577.

Palomeras, I., R. Carbonell, P. Ayarza, M. Fernandez, J. F. Simancas, D. Martínez-Poyatos, F. González Lodeiro, and A. Pérez-Estaún (2011b), Geophysical model of the lithosphere across the Variscan Belt of SW-Iberia: Multidisciplinary assessment, *Tectonophysics*, *508*, 42–51, doi:10.1016/j.tecto.2010.07.010.

Pérez-Estaún, A., J. R. Martínez Catalán, and F. Bastida (1991), Crustal thickening and deformation sequence in the football to the suture of the Hercynian belt of NW Spain, *Tectonophysics*, *191*, 243–253, doi:10.1016/0040-1951(91)90060-6.

Pérez-Estaún, A., J. A. Pulgar, E. Banda, J. Álvarez-Marrón, and the ESCI-N Research Group (1994), Crustal structure of the external variscides in northern Spain from deep seismic reflection profiling, *Tectonophysics*, *232*, 91–118, doi:10.1016/0040-1951(94)90078-7.

Pérez-Estaún, A., J. A. Pulgar, J. Álvarez-Marrón, and the ESCI-N Group (1995), Crustal structure of the Cantabrian Zone: Seismic image of a Variscan foreland thrust and fold belt (NW Spain), *Rev. Soc. Geol. Esp.*, *8*, 307–320.

Pous, J., G. Muñoz, W. Heise, J. Melgarejo, and C. Quesada (2004), Electromagnetic imaging of Variscan crustal structures in SW Iberia: The role of interconnected graphite, *Earth Planet. Sci. Lett.*, *217*(3–4), 435–450, doi:10.1016/S0012-821X(03)00612-5.

Pous, J., et al. (2011), Constraints on the crustal structure of the internal Variscan Belt in SW Europe: A magnetotelluric transect along the eastern part of Central Iberian Zone, Iberian Massif, *J. Geophys. Res.*, *116*, B02103, doi:10.1029/2010JB007538.

Rubio Pascual, F. J., R. Arenas, J. R. Martínez Catalán, L. R. Rodríguez Fernández, and J. R. Wijbrans (2013), Thickening and exhumation of the Variscan roots in the Iberian Central System: Tectonothermal processes and 40Ar/39Ar ages, *Tectonophysics*, *587*, 207–221.

Rudnick, R., and D. Fountain (1995), Nature and composition of the continental crust: A lower crustal perspective, *Rev. Geophys.*, *33*, 267–309, doi:10.1029/95RG01302.

Simancas, J. F., D. Martínez-Poyatos, I. Exposito, A. Azor, and F. Gonzalez Lodeiro (2001), The structure of a major suture zone in the SW Iberian Massif: The Ossa-Morena/Central Iberian contact, *Tectonophysics*, *332*, 295–308, doi:10.1016/S0040-1951(00)00262-6.

Simancas, J. F., et al. (2003), Crustal structure of the transpressional Variscan orogen of SW Iberia: SW Iberia deep seismic reflection profile (IBERSEIS), *Tectonics*, *22*(6), 1062, doi:10.1029/2002TC001479.

Simancas, J. F., P. Ayarza, A. Azor, R. Carbonell, D. Martínez Poyatos, A. Pérez-Estaún, and F. González Lodeiro (2013), A seismic geotraverse across the Iberian Variscides: Orogenic shortening, collisional magmatism, and orocline development, *Tectonics*, *32*, 417–432, doi:10.1002/tect.20035.

Villaseca, C., P. Castiñeiras, and D. Orejana (2014), Early Ordovician metabasites from the Spanish Central System: A remnant of intraplate HP rocks in the Central Iberian Zone, *Gondwana Res.*, doi:10.1016/j.gr.2013.10.007.

Zelt, C., and R. Smith (1992), Seismic traveltime inversion for 2-D crustal velocity structure, *Geophys. J. Int.*, *108*(1), 16–34.